3D-Printed Fluorescence Hyperspectral Lidar for Monitoring Tagged Insects

Hampus Månefjord, Lauro Müller, Meng Li, Jacobo Salvador, Sofia Blomqvist, Anna Runemark, Carsten Kirkeby, Rickard Ignell, Joakim Bood, and Mikkel Brydegaard

***Abstract*—Insects play crucial roles in ecosystems, and how they disperse within their habitat has significant implications for our daily life. Examples include foraging ranges for pollinators, as well as the spread of disease vectors and pests. Despite technological advances with radio tags, isotopes, and genetic sequencing, insect dispersal and migration range remain challenging to study. The gold standard method of mark-recapture is tedious and inefficient. This paper demonstrates the construction of a compact, inexpensive hyperspectral fluorescence lidar. The system is based on off-the-shelf components and 3D printing. After evaluating the performance of the instrument in the laboratory, we demonstrate its efficient range-resolved fluorescence spectra in situ. We present daytime remote ranging and fluorescent identification of auto-powder-tagged honey bees. We also showcase range-, temporally- and spectrally-resolved free-flying mosquitoes, which were tagged through feeding on fluorescent-dyed sugar water. We conclude that violet light can efficiently excite administered sugar meals imbibed by flying insects. Our field experiences provide realistic expectations of signal-to-noise levels, which can be used in future studies. The technique is generally applicable and can efficiently monitor several tagged insect groups in parallel for comparative ecological analysis. This technique opens up a range of ecological experiments, which were previously unfeasible.**

***Index Terms*—Laser radar, fluorescence, hyperspectral sensors, remote sensing, environmental monitoring, instrumentation, ecology, pollination, disease vectors.**

I. Introduction and Motivation

POWDER tagging can be what ring marking is for ornithology, what staining is for microscopy, or what isotopic labelling is for tomography, but for ecological entomology. The ability to mark insects significantly increases detection certainty and specificity compared to classification by intrinsic properties[1], [2], such as cross sections, spectral- or polarimetric properties, and wing beat modulation. In addition, marking allows for the detection of specific individuals, enabling assessment of insect lifetimes[3], population densities[4], and dispersal in the landscape[5], approaches, which have been the cornerstones in numerous entomological studies. Moreover, marking and detecting insects is crucial for monitoring the dispersal and survival of biological control agents in different habitats. In particular, marking and detecting insects have been used to investigate the interaction between predators and parasitoids, as understanding their movement is important for crop management[6]. Powder tagging also enables interaction experiments, involving cross contaminations between, *e.g.,* pollinators and flowers, or as indicators of mating[7]. Except for a few larger species[8], [9], most insects are too small to carry harmonic tags, GPS, or radio devices. Remote sensing, such as radar[10], [11] and lidar[12], [13], can potentially measure insect fluxes in the landscape, but specificity is limited, and flux assessment does not provide information on the migration or dispersal range, or tracking of individuals. Lastly, marking and detection procedures may be used to estimate the population size of insects in a given area.

Lidar is a particularly interesting and efficient active approach to monitor insects[14]. As opposed to sonar, atmospheric attenuation, $\mu_{att.}$, of light can be less than a km^{-1}, and as opposed to radar, the outgoing lidar beam can be collimated. The collimated lidar beam implies that signal loss is dominated by the omnidirectional backscattering, and the attenuation is dependent on the squared return distance, whereas radar typically attenuates by the distance to the fourth power (round trip). The simultaneous ranging and intensity measures of lidar allow the estimation of the fraction of light reaching the aperture and, thus, enable quantification of scattering and fluorescence to some extent[15].

The collimated beam and tunnel vision of lidar systems allow illumination and high detection sensitivity of large probe volumes, even with limited laser power. This is due to the fact that the same light transverses the probed air transect and, thus, light is recycled meter by meter, unless attenuated by an object in the transect. Consequently, entomological lidar[16] yields more observations over time compared to, *e.g.*, sensors or E-traps[17], [18] with a limited probe volume.

Early work demonstrated fluorescence detection of marked insects using lidar [19], but the instrumentation was inefficient in terms of observation counts, and the system was excessively bulky, preventing widespread replication and usage. Over the last decade, topographical lidar technology has undergone

Manuscript received December 13, 2021; revised March 9, 2022; accepted March 22, 2022. Date of publication March 25, 2022; date of current version April 21, 2022. This work was supported by the Swedish Research Council and FORMAS. *(Corresponding author: Hampus Månefjord.)*

Hampus Månefjord, Lauro Müller, Meng Li, Jacobo Salvador, Sofia Blomqvist, Anna Runemark, and Joakim Bood are with the Department of Physics and Department of Biology, Lund University, SE-221 00 Lund, Sweden (e-mail: hampus.manefjord@forbrf.lth.se; lauro.mueller@hotmail.com; meng.li@forbrf.lth.se; jacobo.salvador@forbrf.lth.se; sofia.blomqvist@biol.lu.se; anna.runemark@biol.lu.se; joakim.bood@forbrf.lth.se).

Carsten Kirkeby is with the Copenhagen University, 1165 København, Denmark (e-mail: ckir@sund.ku.dk).

Rickard Ignell is with the Swedish Agricultural University, 23053 Alnarp, Sweden (e-mail: rickard.ignell@slu.se).

Mikkel Brydegaard is with the Department of Physics and Biology, Lund University, SE-221 00 Lund, Sweden, and also with the Norsk Elektro Optikk A/S, 0667 Oslo, Norway (e-mail: mikkel.brydegaard@fysik.lth.se).

Color versions of one or more figures in this article are available at https://doi.org/10.1109/JSTQE.2022.3162417.

Digital Object Identifier 10.1109/JSTQE.2022.3162417

tremendous development and miniaturization. This has offered many novel ecological applications for profiling vegetation structure[20], which affects the abundance and composition of the fauna[21], and can now be used to assess insect defoliation[22]. The depth information gained from airborne lidars yields complementary information to hyperspectral imaging, discriminating molecular compositions. Examples are today well-established on satellites, airplanes, and drones[23], [24].

The need for improved specificity has spurred the development of multiband lidar[*e.g.*, 25, 26], and extensive efforts for combining data from vegetation lidar and hyperspectral imaging have been conducted[*e.g.*, 27]. The method of fusing lidar and hyperspectral imaging signals is challenging, since the harmonic pulses of the lidar at distinct ranges are difficult to match to individual pixels of the hyperspectral image. Advanced multiband lidar concepts, including fluorescence lidar have been presented over the last two decades[28]–[32]. These time-of-flight systems are based on pulsed solid-state lasers and ultraviolet harmonics through gated-imagers, spectrometers, or multi-anode PMT arrays. None of these concepts provide at the same time: a) full-waveforms range echo, b) hyperspectral signatures, and c) continuous time series.

Full waveform hyperspectral short-range time-of-flight lidars have been reported based on super-continuum sources[33], [34]. Such fiber lasers are, however, limited to low peak powers and high repetition rates, and the approach can therefore not be scaled up to long-range remote sensing, because the maximum unambiguous range is the speed of light over twice the repetition rate. This limitation does not exist for continuous-wave Scheimpflug lidars[35]. Scheimpflug lidars can be rescaled to cover both short[36] and long ranges[37]. The Scheimpflug method can be extended to full waveform real-time hyperspectral lidar based on image sensors and laser diode devices[38], [39]. Applications have included aquatic profiling[40] and vegetation profiling from drones[41].

In this work, we further develop the design principles of fluorescence hyperspectral Scheimpflug lidar, and demonstrate a compact, low-cost instrument built with off-the-shelf components and 3D printing. Compared to previous aquatic work based on blue 445 nm lasers and shorter ranges, this instrument is based on violet laser at 401 nm and working distance up to 100 m in air. We show that fluorescence can simultaneously be resolved in range, time, and photon energy (wavelength) from free-flying tagged insects in full sunlight. Furthermore, we demonstrate the feasibility of detecting insects fed by a fluorescent sugar solution.

II. Instrument Design

Here, we present the initial design considerations, raytracing optimization, and the fabrication with 3D printed parts. The complete system overview is provided in Table I.

A. First-Order Design

The fluorescence hyperspectral lidar derives from earlier projects of Scheimpflug lidar[36], [42], [43], and its hyperspectral variety[44], [45], as well as the geometry and design details have been thoroughly revised[35], [46], [47]. Hyperspectral Scheimpflug lidar is based on the combination of Scheimpflug lidar and hyperspectral push-broom imaging[48].

TABLE I
System Specifications of the Fluorescence Hyperspectral Lidar

Parameter	Symbol	Quantity	Unit
Transmitter			
Transmitted wavelength	λ_{ex}	401	nm
Lidar power	P	1	W
Expander diameter	$Ø_{exp}$	25	mm
Expander focal length	F_{exp}	75	mm
Slant angle	φ	0..3	°
Laser chip size		3x50	µm
Beam divergence (transversal)		0.4	mrad
Beam convergence (baseline axis)		0.15	mrad
Receiver			
Receiver diameter	$Ø_{rec}$	75	mm
Receiver focal length	F_{rec}	300	mm
Field-of-View	FoV	0.7x57	mrad
Range	r	5..100	m
Range resolution	Δ_r/r	5..10	%
Range of half overlap	r_0	11	m
Shape factor	γ	7	
Spectral analyzer			
Spectral range	λ	400..800	nm
Spectral resolution	$\Delta\lambda$	~6.7	nm
Slit-imager magnification	M	2:1	
Number of effective bands		71	#
Slit width		200	µm
Imager			
Pixel pitch	ℓ_{pix}	5.89	µm
Number of pixels	N_{pix}	1920x1200	#
Max sample rate	f_s	124	Hz
Signal-noise ratios demonstrated	SNR	22..950	
Dynamic range		12	bits
System			
Baseline separation	D	324	mm
Slit tilt	α	39.5	°
Power consumption (not PC)	P_{tot}	11	W
System footprint (not PC)		30x50x9	cm
Weight (not PC)		~3	Kg
Bill of materials (not PC)		~2715	€

Briefly, the Scheimpflug principle[49] allows sharp focusing across wide ranges despite using a large aperture. This is accomplished by letting the object plane, the lens plane, and the image plane intersect. For a Scheimpflug lidar, the object plane is comprised of an air transect illuminated by a laser beam (see Fig. 1a). In addition to the Scheimpflug condition, which does not consider focal lengths, the so-called hinge rule relates the focal plane of the optics to the object- and image planes (see Fig. 1a).

As a rule of thumb, a larger tilt of the detector (here slit) -plane implies a decreased triangulation resolution. A benefit, however, is a shorter lidar baseline, and, thus, a more compact system. We designed our lidar to cover a range from 5 m to 100 m, which was accomplished by an f300 mm, ø75 mm receiver achromat, a transmitter-receiver baseline separation, D, of 32.4 mm, a slit tilt angle, α, of 39.5°, and a slant angle, φ, of 2° (the angle between the optical axis of the transmitter and receiver).

Spectral dispersion of received light is accomplished perpendicularly to the ranging axis (see spectral analyzer sketch in Fig. 1b). We employed the prism-grating-prism (PGP) method[48], with an ensemble of an f100 mm achromat, a 6° wedge, a 300 groove/mm transmission grating, a 4° wedge, and an f50 mm achromat. The purpose of the two wedges is

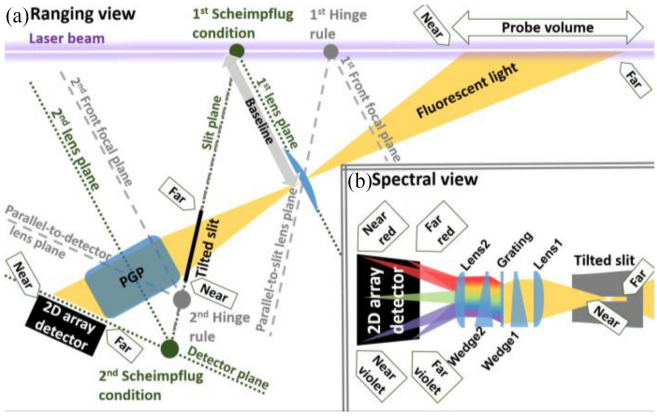

Fig. 1. a) First-order design approach to hyperspectral lidar using two consecutive sets of Scheimpflug conditions and hinge rules. The first Scheimpflug condition relates the violet laser beam to the receiver lens- and slit-plane, whereas the second Scheimpflug condition relates the slit-plane to the spectrometer- and detector-plane. Note that the angle between the receiver and the laser axes is exaggerated in this drawing. In reality, it is approximately 2˚, which elongates the probe volume. b) Orthogonal sketch showing the dispersion of photon energies by a prism-grating-prism method (PGP).

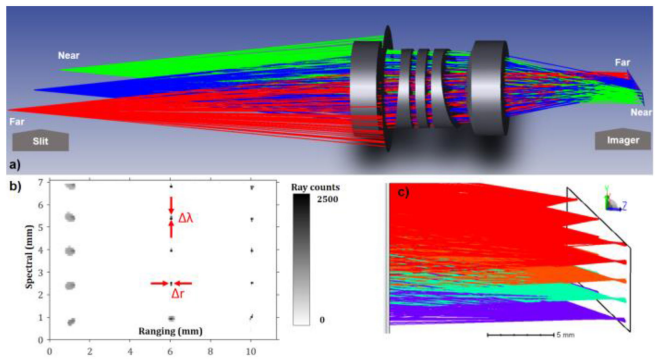

Fig. 2. Screenshots from raytracing simulation and optimizations of the spectral analyzer. a) From left; polychromatic light-cone point sources at three positions along the tilted slit propagate through the prism-grating-prism assembly and form a range-photon energy image on the imager. The colors of the rays represent the different source points along the slit b) Point spread functions of the ray bundles across the imager. c) Close-up of beam waists or ray bundles, the focus for closer ranges was down-prioritized since the triangulation principle of bistatic lidars counteract this effect. The colors of the bundles represent [as opposed to in (a)] the wavelength of the light.

to get the optimal incidence angle of the light onto the blazed grating, while keeping the optical path coaxial.

The f-number of the spectrometer optics needs to be smaller than the f-number of the collecting optics to capture the light cone across the slit efficiently. Systems covering one octave (*e.g.*, 400-800 nm), such as the one presented here, require gratings with the lowest available groove per millimeter. In order to fit the entire spectral range onto our imager (Sony IMX174 CMOS in a Basler acA1920-155 um camera), the setup required a slit-to-imager magnification of 2:1. This suggests a detector tilt of 39.5°/2 ≈ 20°. Since the area of the imager is 11.3 mm x 7.1 mm, the magnification implies that 22.6 mm of the slit is imaged onto the imager. To accomplish a decent signal strength at fast sample rates, we chose a moderate spectral resolution with a slit width of 200 µm. Considering the magnification of the spectral analyzer, this potentially provides 2·7.1 mm/200 µm = 71 effective spectral bands across the imager.

B. Raytracing

The Scheimpflug condition and hinge rule are similar to the first order reciprocal truncation, the thin lens formula. In practice, the achromats, wedges, and grating account for several cm of glass with different refractive indices. Consequently, the optimal design deviates substantially from thin lens approximations. Raytracing was implemented in OpticStudio (Zemax, USA) to model the light through the spectral analyzer. The initial setup was based on the Scheimpflug- and hinge rules, as described in the previous section. The raytracing used three F/4 light cones sources from the near, middle, and far end of the slit as sources. Each source consisted of five wavelengths, 400, 480, 560, 640, 720, and 800 nm. In total 15 ray bundles impinged on the imager, three along the ranging axis, and five along the spectral axis (Fig. 2).

The distance and the tilt of the imager were adjusted to minimize the point spread function of all 15 ray bundles ($\Delta\lambda$ and Δr in Fig. 2b). In practice, the point solutions are convoluted by the imaged slit width (100 µm). Thus, the spot size should ideally match this size in the spectral domain. Since Scheimpflug lidar is based on the triangulation principle, range resolution deteriorates with range. Therefore, focusing in the ranging domain should be prioritized for the far end of the imager (Fig. 2b and 2c). Stray light, ghost reflections, and the 0^{th} diffraction order from the grating could also be traced. This was, however, not pursued in this initial test.

C. 3D Printed Spectral Analyzer

The spectral analyzer is comprised of five optical elements of various shapes, with minimal spacing. Mounting them with conventional photonic lab supplies would be both challenging and costly. Furthermore, precise alignment of the pieces would not be guaranteed. Instead, we proceeded with the optimized parameters from the raytracing and designed a sandwich structure for additive filament 3D printing. The sandwich concept implies cutting the envisioned optical design into two similar blocks, in which the optical path and slots for the optical components were removed.

3D printing offers numerous simplifications over conventional optical design approaches, such as CNC milling. Considerations, such as the effects of the size of the milling tool, and the problem of milling right-angle corners are not present in the additive manufacturing. Precise baffles, matching the light cones, were added along the optical path in order to prevent forward scattered light.

The sandwich structure was printed in black PLA (PLA-DF02, Dremel, USA), with a fill factor of 100% on a commercial 3D printer (Dremel 3D45, USA) with 200 µm layer height. The used filament was opaque but glossy. We learned that a limited number of baffles, spaced along the light pipe, was optimal for suppressing stray light. In addition, maximal internal fill factor was not required. The structural integrity was ensured by steel rods through the assembly, see Fig. 3. Carbonized and antistatic alternative filaments, which could reduce the glossiness are available at a higher cost.

After the initial 3D-printing trials, dimensions for screw- and rod holes, and the slots for optical elements, had to be adjusted

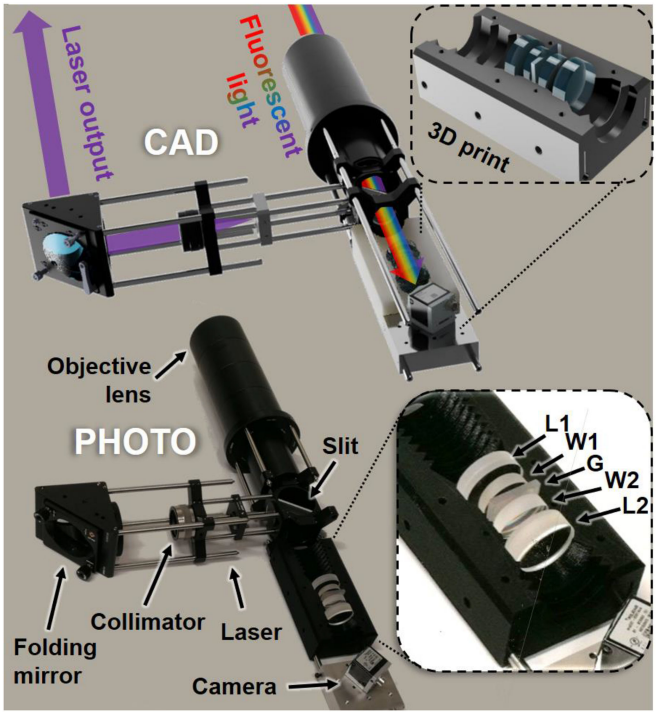

Fig. 3. CAD drawing and photograph of the complete hyperspectral lidar, partly made from a commercial optical cage system, with precision kinetic mechanisms for aligning beam field of view overlap and divergence, as well as slit positioning. The 3D-printed sandwich structure (seen in the two insets) had its top part removed to reveal the lenses L1 and L2, wedge prisms W1 and W2 and the transmission grating G. .

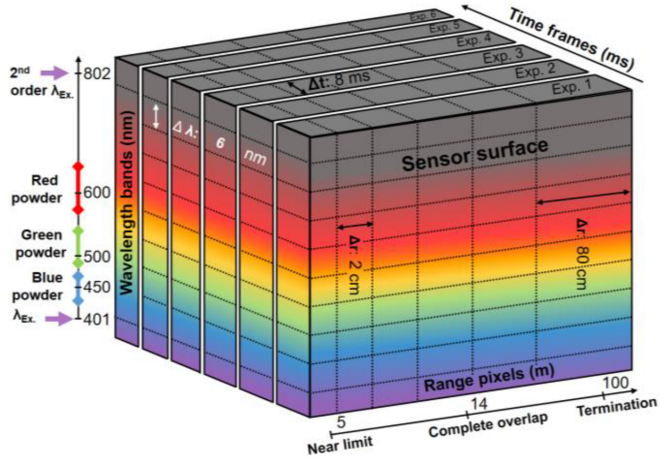

Fig. 4. The data acquired by the hyperspectral lidar contains information about range and wavelength, which are imaged onto the horizontal and vertical direction of the imager. Time is resolved by stacking camera exposures. The resolution and range in the three dimensions are indicated in the figure. Specific system values are indicated, such as the wavelength of the laser and the fluorescent powders used, the near limit, the range of complete overlap, and the position of the termination board.

with a margin for the nozzle width of the 3D printer. The precision, structural stability, and rigidness of the spectral analyzer sandwich structure were satisfactory. Long-term degradation seems unlikely because a steel rod cage system was embedded along the optical path, and steel bolts clamped the two sandwich parts together. Fig. 3 displays the 3D model, and the prototype of the entire lidar, including the bottom part of the spectral analyzer, revealing the internal optical elements.

III. Calibration and Performance

The hyperspectral lidar acquires backscattering and fluorescence intensity counts (12 bit), as a function of time, distance, and photon energy (see Fig. 4). The spectral range covers the excitation wavelength, the fluorescence spectra of different powder dyes, and the entire visible range. The spectral range also includes the second-order diffraction of the excitation wavelength, which may be used as spectral calibration. The time-domain information is acquired as a sequence of images, and the frame rate is limited by the exposure time and the USB3 transfer speed.

Our customized acquisition program was made in LabVIEW (National Instruments, USA). The program acquires a sequence of images, with parameters, such as the number of images, their binning, exposure time, and gain, being real-time customizable. The collected sequence of images, in the form of a data cube (see Fig. 4), is visualized in the interface of the program. The mean image, averaged over time, the lidar echo (intensity *vs*. range) of selected spectral bands, the average spectrum of a selected range region, and a time-range map are all visualized, while the system acquires the lidar signal. The image cubes are then continuously saved as raw files, with time-stamped filenames.

A. Spectral Calibration

A spectral calibration procedure investigated the mapping from pixel number to wavelength, in nanometer, along the spectral dimension. The spectral analyzer was removed from the lidar system, and the slit was directed towards an ø200 mm integration sphere coated with $BaSO_4$ (Oriel, USA). Light from a spectral cadmium (Cd) lamp, with known spectral lines, was injected into the sphere through another port. The sphere provides a homogenous Lambertian light field. The resulting intensity image on the imager can be seen in Fig. 5a. Four atomic cadmium spectral lines are observed with wavelengths of 467.8, 480.0, 508.6, and 643.8 nm (Fig. 5d). The full width at half maximum (FWHM) of the 5s5p-5s6s transition (508.6 nm) was measured satisfactory at the far- and mid-range of the slit to 5.5 and 7.6 nm. However, in the near range, the spectral resolution deteriorated to 30 nm.

For the same atomic line, the shift of the spectral registration along the range axis was studied, by finding the center of mass (CoM) and the standard deviation (SD) of the signal (Fig. 5c). The CoM and SD account for the first two statistical moments, and are used to quantify spectral misregistration effects, such as keystone and smile[50]. The pixel-to-wavelength mapping could best be described by first-order polynomials. The first coefficient varied from 348 to 338 nm from the near to the far end of the imager, and the second polynomial coefficient varied from 0.369 to 0.385 nm/pixel. This change in the polynomial coefficients quantifies the keystone effect. The coefficients varied linearly across the range, thus, no smile was detected. Correcting the artifact by image transformation, and wrapping, induces interpolation errors. Another approach would be to use range-dependent spectral calibration.

In situ, the lidar provided an auto-calibration feature; both the elastic (401 nm) backscattering from the atmosphere, and its

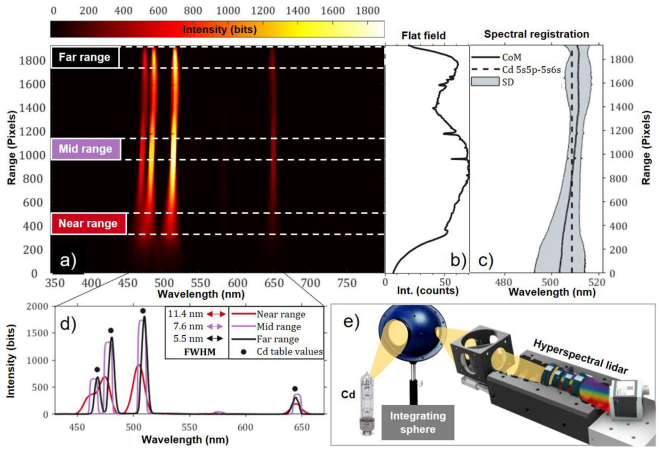

Fig. 5. Laboratory calibration and performance tests. a) Light distribution on the CMOS image chip when the spectral analyzer was presented with a homogeneous light-field of a cadmium (Cd) spectral lamp. b) The mean intensity along the ranging direction of the hyperspectral lidar was obtained by averaging over the complete spectral range. The intensity goes down in the extreme ends of the range, and its shape changes slightly with the positioning of the spectral analyzer relative to the integrating sphere port. c) The spectral registration of light from the 508.6 nm atomic line (the Cd 5s5p-5s6s transition) is described with the center of mass (CoM) and standard deviation (SD) of intensity on the imager. d) The spectrum of the spectral cadmium lamp is shown for the far, mid, and near range as indicated in (a). A shift in the peak wavelength and the smearing of the 467.8 and 480.0 nm lines can be seen for the near range, and smearing increases further at the extreme near range. e) The experimental configuration included a Cd spectral lamp illuminating an integrating sphere, and the spectral analyzer was directed toward another port of the sphere.

second-order diffraction (fake 802 nm light), was observable as two narrowband signals. Spectral calibration was thus always available as an interpolation between these lines.

B. White Calibration

The spectral response of the instrument is primarily governed by the spectral sensitivity of the CMOS imager, and the efficiency curve of the grating. Light from a halogen tungsten filament was injected into the integrating sphere. The source spectrum was assumed to be a 3000 K Planck black body distribution. The measured peak response was identified in the 500-600 nm region, but sensitivity extended over the full spectral range. The response was ∼25% of the peak value in the extremes at 400 nm and 800 nm. This suppression was somewhat beneficial, since no suppression filter for the elastic excitation light was used, which is desirable when capturing elastic and fluorescence light within the same dynamic range. A steep spectral response will have the effect of shifting observed fluorescence features towards the center if not compensated for. In our case, however, this effect was minimal.

C. Flat Field Calibration, Lidar Form Factor, and Cross-Sections

The homogeneous light field from the integrating sphere measurements provides the intensity along the slit (Fig. 5b). A partial shielding of the light cones, at the extremes of the slit, resulted in an attenuation of the response at the outermost near and far ends. The effect could be addressed by lowering the f-number of the spectral analyzer or by reducing the slit-detector

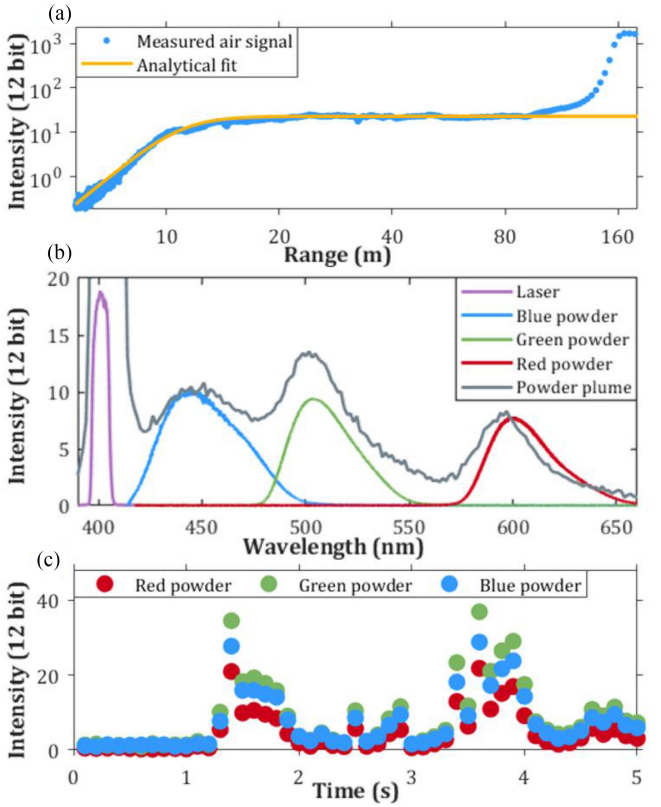

Fig. 6. a) Elastic backscattering lidar signal from the air. The lidar transect is terminated at a board 166 m away. The analytical function (1) is fitted to the air signal with $r_0 = 11$ m and $\gamma = 7$. b) Remotely retrieved spectrum for the powder plume containing elastic backscattering, and fluorescence from released plume of all three powders; the axis indicates lidar intensity counts. The individual spectra of the laser, and each powder, as measured with a compact spectrometer in the lab. c) The average intensity of the recorded fluorescence of each powder over time near the release point of the plume.

magnification. We noted from Fig. 5b that at least 85% of the imager could be used in the ranging domain.

The actual range response of the lidar in the field was a combined effect of the aforementioned flat-field calibration and the beam-FoV overlap. The curve can be expressed analytically[51], although the gold standard[52] is to use the tabulated Raman cross-section of a bulk signal of, *e.g.*, N_2, O_2 (or H_2O in aquatic lidar). Instead, we used a previously described analytical model for Scheimpflug lidars[53],

$$G_{overlap(r)} = \frac{1}{1 + \left(\frac{r_0}{r}\right)^{\gamma}} \tag{1}$$

Here, r_0 is the range of half overlap, and γ is a shape factor. In the field, the lidar provides an intrinsic form-factor calibration, since the homogenous and static air signal will continuously report the system-range sensitivity curve. We used this elastic air signal from the field experiment (see Fig. 6a), and identified $r_0 = 11$ m and $\gamma = 7$. The intensity counts of the measured air signal at 50 m range averaged 21 counts, while the noise (SD over time) was 0.96 counts. This gives a signal-to-noise ratio (SNR) of 22.

Whereas the air signal can be flat beyond complete overlap (as seen in Fig. 6a), fluorescent echoes from solid targets will decrease by r^2. It is possible to compensate for the r^2 decrease to

some extent by the increasing slope of Eq. 1. However, the field of quantitative fluorescence cross-sections is poorly developed, possibly due to the scarce availability of fluorescence lidars. More details on elastic lidar cross-sections can be found in[53].

D. Range Calibration

The Scheimpflug range calibration relies on precise geometric information about the system. A position along the slit is converted into an observation angle with the receiver lens as a pivot. The range can then be estimated by triangulation, given that the baseline separation and the observation angle are known. The range for each pixel, $r_{pix,}$ is described by

$$r_{pix(n)} = D\frac{F_{rec} + nM\ell_{pix}\left(\sin\alpha - \cos\alpha\cot\varphi\right)}{F_{rec}\cot\varphi + nM\ell_{pix}\left(\sin\alpha\cot\varphi + \cos\alpha\right)} \quad (2)$$

in which D, F_{rec}, M, ℓ_{pix}, α, and φ are system parameters found in Table I, and n is a running index from 1 to N_{pix}. The details and derivation of Eq. 2 are found in[47]. The pixel-to-range mapping can, however, also accurately be approximated by a squared relation[46]. The ranging accuracy deteriorates with range. However, ranging precision can be improved at far ranges, at the expense of range precision in the short range, by choosing an adequate beam expander aperture and a convergent beam[35], [54]. Consequently, the range resolution can deteriorate linearly. We estimate the ranging accuracy to approximately 6% for the present system.

IV. Examples of Field Applications

Several field applications were investigated at Stensoffa Field Station located in southern Sweden. The fluorescence hyperspectral lidar was mounted on an astronomical tripod (EQ8, SkyWatcher, Canada) placed in a carport tent for weather protection.

A. Powder Plume Releases

Plume-release experiments are often performed within different variations of lidar research. Such experiments can have several different purposes, *e.g.,* characterizing a lidar system or examining the measurement possibilities for a specific lidar. Other possibilities include fundamental research, *e.g.*, in studies of biological aerosols or to detect biological warfare agents [see, e.g., 31 and references therein]. Measurements in plumes of different particles and smoke have also been performed with Scheimpflug lidar to investigate the potential for particle classification and sizing[55], [56].

In the present work, as an initial proof-of-concept study, released plumes of mixed fluorescent powders were investigated with the Scheimpflug-lidar system. An equal mixture of red, green, and blue fluorescent powder (UV Holi powder, Paint-Glow, U.K.) was released in the vicinity of the lidar transect. The imager was set to 100 ms exposure time, a gain of 24 and 2x4 binning (4 along the spectral axis). The spectral intensity profile of the powder mixture was captured at the range of release 50 m from the lidar at a single exposure (Fig. 6b). The intensity variation at the release point over time was recorded (Fig. 6c).

B. Powder Tagged Bees for Foraging Range Assessment

Pollination is an ecosystem service, which is crucial for food production[57]. By marking bees from known hives and tracking them over fields, we can gain fundamental insights into their ecology, facilitating the use of beehives as pollination services. Moreover, in the face of insect decline[58]–[61], a solid understanding of how honey bees impact wild pollinators is crucial for maintaining pollination services from wild insects. Powder tagging provides a powerful tool to study interactions between bees from specific hives and untagged wild insects. Several hives could also be distinguished by tagging with spectrally distinct fluorescent powder to study how spatial distributions from hives perturb each other. This approach, hence opens up novel research questions on species interactions.

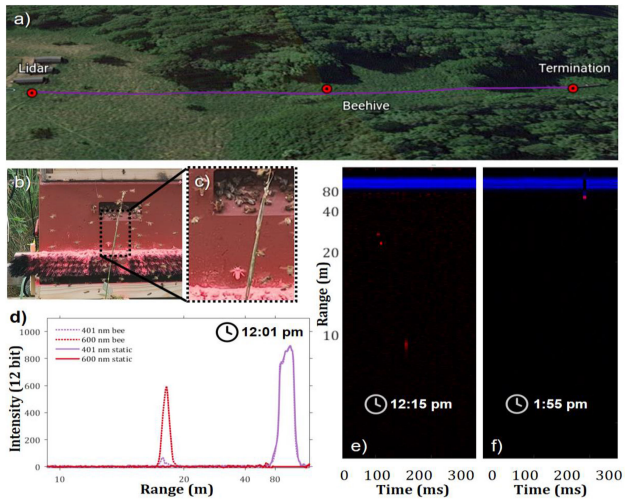

Fig. 7 a) The lidar transect over a meadow at Stensoffa field station. The beam was terminated 100 m from the lidar. Forest surrounds the transect, but no trees are in the vicinity of the beam. A beehive with a fluorescent marking tray was located at 55 m from the lidar at the ground, 1 m below the beam. b) The beehive with the attached powder tray and a broom. c) Several powdered bees are flying around the hive. d) The signal acquired by the hyperspectral lidar shown as an echo for a time during which a bee is in the beam, and a static time during which nothing is obstructing the beam before the termination. For both instances, the elastic signal (397-406 nm) and the red fluorescent signal (585-615 nm) are shown in violet and red, respectively. The SNR of the fluorescent signal was 177 compared to 20 of the elastic. e,f) Two selected occurrences of marked bees entering the beam during full daylight. The intensities of the red and elastic spectral band are shown as the red and blue channels of the RGB image, in which the axes represent time and range. A reduction of the elastic termination signal is seen at the same time of the bee occurrence in e), which is caused by the extinction cross-section of the bee in the beam.

In this work, a powder-marked bee monitoring experiment was conducted. The lidar transect spanned a meadow of varying vegetation, before reaching a laser beam termination screen 100 m away. A beehive was situated at 55 m along the lidar transect (Fig. 7a).

Auto-marking of the bees was accomplished by attaching a tray with red dye powder under the entrance of a beehive; similar methods have been applied in previous work[62]. In our implementation, a powdered broom was mounted above the entrance to ensure automatic marking of bees as they departed from the hive (Fig. 7b and 7c).

The experiment was conducted over three days, and the powder tray was refilled each morning at 7:30 am. Subsequently, the hyperspectral lidar was started. The lidar collected data during the day until 8 pm, at which time no more honey bees were active. Several marked bees were observed with the lidar, corresponding to registered occurrences in time-range plots (Fig. 7e and 7f), or

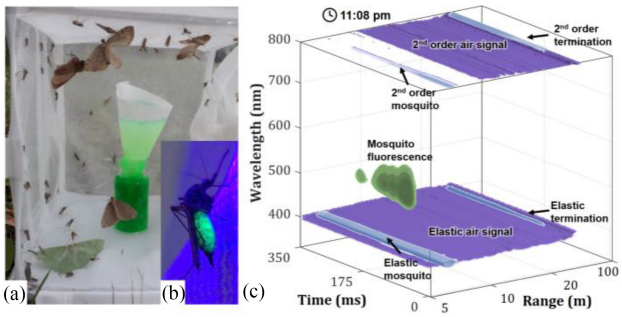

Fig. 8. a) Insects collected from a CO_2 trap were moved to a cage with a dyed sugar solution. b) A mosquito fed with fluorescent sugar water, lit by a violet torch. c) A released marked mosquito entered the lidar beam. The resulting signal is presented as colored iso-surfaces in time, range and wavelength, which is the full data cube collected by the lidar (compare to Fig. 4).

echoes in range-intensity diagrams (Fig. 7d). The imager was set to 124 Hz framerate, 7 ms exposures, 24 gain, and 4x4 binning. The fluorescence signal from the bee corresponding to the echo shown in Fig. 7d peaked at 595 intensity counts, averaged over a red spectral window from 585 nm to 615 nm. The noise (SD) of this window was 3.4 counts, which gives an SNR of 177. From the insignificant reduction of the termination echo, we understand that this individual bee intersects the beam peripherally.

C. Sugar Feeding With Fluorescence Dyes

Previous studies have used sugar feeding to mark insects, *e.g.*, to monitor the proportion of released sterile mosquitoes, both with radioactive isotopes[63], fluorescent markers[64], of which some can even mark the seminal fluid of males, facilitating monitoring of mosquito mating behavior, and non-fluorescent markers[65]. Sugar feeding has also been used to kill insects with toxic baits[66].

One of the most valuable aspects of marking insects alive, and then releasing and detecting them again, is to estimate the population size in a habitat[6]. This method can provide insight into the effectiveness of control measures, such as bed nets and the removal of breeding sites for specific species of mosquitoes.

In our work, a combined light- and CO_2-trap (Model 1212, John W. Hock Company, USA) was operated near a lakeshore inside the forest at Stensoffa, approximately 100 m from the lidar beam, shielded by trees. The trap was baited with CO_2, from dry ice, and set overnight 6:00 pm, 9th August 2021. The live catch was emptied into a cage the following day at 8:00 am. The catch contained predominantly mosquito species, but also moths and blackflies (Fig. 8a). The species were kept in the cage over the day along with a vial of 10% sugar solution with a dissolved green fluorescence marker pen (Q-connect, Belgium), and a coffee filter, allowing the insects to land and feed on the solution (Fig. 8a). Using a violet (405 nm) LED torch, we could verify that both mosquitoes and moths had fed from the sugar solution, by the green fluorescence in their abdomen (see Fig. 8b).

At 11:00 pm the fluorescent sugar-fed specimens were carefully released one by one under the beam at 15 m distance from the lidar. The specimens were detected directly upon their release, and at later instances when transiting the beam again. Fig. 8c displays one case of a free-flying sugar-fed mosquito entering the beam. The visualization displays registered light intensity as a function of time, range, and wavelength (photon energy). Semi-transparent iso-surfaces at 500, 1000, 1500, and 2000 counts encircles the green fluorescence at 12 m, the elastic backscattering from the mosquito, the elastic air scatter, and the termination at 100 m distance. The imager was operated at 124 Hz frame rate, 7 ms exposures, 24 gain, 4x2 binning (4 in the spectral axis). The fluorescence peak signal was at 3794 intensity counts in a single spectral band, and the noise amplitude with the same settings was 1.3 counts. Thus, the SNR was 3015 at 12 m distance. Considering the form factor, and the $1/r^2$ attenuation, we estimate that we could detect such signals at 458 m with an SNR of 2:1. This is, however, beyond the design range of our system.

V. Conclusion and Outlook

In this work, a hyperspectral lidar has been presented with a detailed discussion on its design and assembly. The material costs amounted to ∼2715 € and the weight ∼3 kg (excluding acquisition computer and tripod). For comparison, fluorescence lidars reported a decade ago had material costs of more than a million euros and weights of several tons[19], [31]. Since then, smaller systems were reported[30], still with a solid-state laser of around one hundred kg. A previously reported pulsed lidar[19] operated at 10 Hz (100 ms between pulses), and since insect transit times can be expected to be less than 10 ms the insect count was low. The low price of the present system opens up possibilities for, *e.g.,* larger-scale future comparative studies using multiple lidar systems or *in situ* implementation in low-income countries. The portability of the system enables not only placement on astronomical tripods, but also mounting on drones[45], vehicles, or in hiking backpacks could be envisioned.

The performance of the hyperspectral lidar was tested in the field for multiple fluorescence applications with excellent SNR even during full daylight, which is generally a challenge even for pulsed fluorescence lidars. Usage of our lidar in ecological studies has the potential to reduce the labor-intensive mark-recapture studies of insects. We have demonstrated that multiple methods of fluorescent marking (exterior-powder-tagging and ingestion) are feasible with the lidar, which could yield complementary ecological information. Possible biases of this technique include affecting the behavior of the studied insects by the tagging powder. This also applies in non-lidar-based marking studies. Still, a higher amount of powder yields a stronger lidar echo but could affect the insects more severely. The mass powder tagging lifetime of bees was previously estimated to 4 days [67], compared to our study bees retag themselves multiple times per day and laser induced fluorescence is expected to be more sensitive than the naked eye. Another challenge is that the violet 401 nm light from the laser is visible to most insects and could imply a bias in nocturnal monitoring.

Other inelastic applications such as autofluorescence of chlorophyll in vegetation or Raman scattering for various uses could be envisioned for the instrument without modifications. CAD drawings, a component list, driver circuit, and acquisition software can be provided upon request from the corresponding author.

References

[1] A. P. Genoud *et al.*, "Identification of gravid mosquitoes from changes in spectral and polarimetric backscatter cross-sections," *J. Biophoton.*, 2019, Art. no. e201900123.

[2] M. Li *et al.*, "Bark beetles as lidar targets and prospects of photonic surveillance," *J. Biophoton.*, vol. 14, no. 4, 2021, Art. no. e202000420.

[3] M. Sielezniew, A. Kostro-Ambroziak, and Á. Kőrösi, "Sexual differences in age-dependent survival and life span of adults in a natural butterfly population," *Sci. Rep.s.*, vol. 10, no. 1, pp. 1–10, 2020.

[4] L. M. Torres-Vila *et al.*, "Assessing mass trapping efficiency and population density of Cerambyx Welensii Küster by mark-recapture in dehesa open woodlands," *Eur. J. Forest Res.*, vol. 131, no. 4, 2012, pp. 1103–1116.

[5] C. Kirkeby *et al.*, "Quantifying dispersal of european culicoides (Diptera: Ceratopogonidae) vectors between farms using a novel mark-release-recapture technique," *PloS One*, vol. 8, no. 4, 2013, Art. no. e61269.

[6] B. Lavandero, S. Wratten, J. Hagler, and M. Jervis, "The need for effective marking and tracking techniques for monitoring the movements of insect predators and parasitoids," *Int. J. Pest Manage.*, vol. 50, no. 3, pp. 147–151, 2004, doi: 10.1080/09670870410001731853.

[7] J. W. Crenshaw Jr, "The life history of the southern spiny lizard, sceloporus undulatus undulatus latreille," *Amer. Midland Naturalist*, 1955, pp. 257–298.

[8] R. S. Pasquet *et al.*, "Long-distance pollen flow assessment through evaluation of pollinator foraging range suggests transgene escape distances," *PNAS*, vol. 105, no. 36, pp. 13456–13461, 2008.

[9] O. Ovaskainen *et al.*, "Tracking butterfly movements with harmonic radar reveals an effect of population age on movement distance," *PNAS*, vol. 105, no. 49, pp. 19090–19095, 2008.

[10] G. Hu *et al.*, "Mass seasonal bioflows of high-flying insect migrants," *Science*, vol. 354, no. 6319, pp. 1584–1587, 2016.

[11] V. A. Drake and H. Wang, "Ascent and descent rates of high-flying insect migrants determined with a non-coherent vertical-beam entomological radar," *Int. J. Remote Sens.*, vol. 40, no. 3, pp. 883–904, 2019.

[12] Y. Li *et al.*, "Insect flight velocity measurement with a CW near-IR scheimpflug lidar system," *Opt. Exp.*, vol. 28, no. 15, pp. 21891–21902, 2020.

[13] S. Jansson *et al.*, "Real-time dispersal of malaria vectors in rural africa monitored with lidar," *PLoS One*, vol. 16, no. 3, 2021, Art. no. e0247803.

[14] M. Brydegaard and S. Svanberg, "Photonic monitoring of atmospheric and aquatic fauna," *Laser Photon. Rev.*, 2018, vol. 12, Art. no. 1800135.

[15] V. A. Kovalev and W. E. Eichinger, *Elastic Lidar: Theory, Practice, and Analysis Methods*. Hoboken, NJ, USA: Wiley, 2004.

[16] M. Brydegaard *et al.*, "Lidar reveals activity anomaly of malaria vectors during pan-African eclipse," *Sci. Adv.*, vol. 6, no. 20, 2020, Art. no. eaay5487.

[17] K. Rydhmer *et al.*, "Automating insect monitoring using unsupervised near-infrared sensors," 2021, *arXiv:2108.05435*.

[18] I. I. Rigakis *et al.*, "The e-funnel trap: Automatic monitoring of lepidoptera; a case study of tomato leaf miner," *Comput. Electron. Agriculture*, vol. 185, 2021, Art. no. 106154.

[19] Z. Guan *et al.*, "Insect monitoring with fluorescence lidar techniques: Field experiments," *Appl. Opt.*, vol. 49, no. 29, pp. 1–11, 2010.

[20] M. A. Wulder *et al.*, "Lidar sampling for large-area forest characterization: A review," *Remote Sens. Environ.*, vol. 121, pp. 196–209, 2012.

[21] X. Guo *et al.*, "Regional mapping of vegetation structure for biodiversity monitoring using airborne lidar data," *Ecological Inform.*, vol. 38, pp. 50–61, 2017.

[22] R. Meng *et al.*, "Mapping canopy defoliation by herbivorous insects at the individual tree level using bi-temporal airborne imaging spectroscopy and LiDAR measurements," *Remote Sens. Environ.*, vol. 215, pp. 170–183, 2018.

[23] P. S. Thenkabail and J. G. Lyon, *Hyperspectral Remote Sensing of Vegetation*. Boca Raton, FL, USA: CRC, 2016.

[24] J. P. Arroyo-Mora *et al.*, "Assessing the impact of illumination on UAV pushbroom hyperspectral imagery collected under various cloud cover conditions," *Remote Sens. Environ.*, vol. 258, 2021, Art. no. 112396.

[25] N. Ekhtari, C. Glennie, and J. C. Fernandez-Diaz, "Classification of airborne multispectral lidar point clouds for land cover mapping," *IEEE J. Sel. Topics Appl. Earth Observ. Remote Sens.*, vol. 11, no. 6, pp. 2068–2078, Jun. 2018.

[26] S. Kaasalainen, "Multispectral terrestrial lidar: State of the art and challenges," *Laser Scanning*, vol. 14, pp. 5–18, 2019.

[27] T. Sankey *et al.*, "UAV lidar and hyperspectral fusion for forest monitoring in the southwestern USA," *Remote Sens. Environ.*, vol. 195, pp. 30–43, 2017.

[28] S. Svanberg, *Fluorescence Spectroscopy and Imaging of Lidar Targets*. in L. R. Sensing, T. Fujii, and T. Fukuchi, Eds. Boca Raton, FL, USA: CRC, 2005, pp. 433–467.

[29] V. Raimondi *et al.*, "The fluorescence lidar technique for the remote sensing of photoautotrophic biodeteriogens in the outdoor cultural heritage: A decade of in situ experiments," *Int. Biodeterioration Biodegradation*, vol. 63, no. 7, 2009, pp. 823–835.

[30] V. Raimondi, C. Conti, D. Lognoli, and L. Palombi, "Latest advancements in fluorescence hyperspectral lidar imaging of the cultural heritage," in *Fundamentals of Laser-Assisted Micro-And Nanotechnologies*, vol. 9065, Bellingham, WA, USA: SPIE, Nov. 2013, pp. 274–284.

[31] NATO, *Laser Based Stand-Off Detection of Biological Agents*. Washington, DC, USA: North Atlantic Treaty Organisation, 2010.

[32] M. Sasano, *et al.*, "Development of a regional coral observation method by a fluorescence imaging LIDAR installed in a towable buoy," *Remote Sens.*, vol. 8, no. 1, 2016, Art. no. 48.

[33] T. Malkamäki, S. Kaasalainen, and J. Ilinca, "Portable hyperspectral lidar utilizing 5 GHz multichannel full waveform digitization," *Opt. Exp.*, vol. 27, no. 8, pp. A468–A480, 2019.

[34] T. Hakala *et al.*, "Full waveform hyperspectral LiDAR for terrestrial laser scanning," *Opt. Exp.*, vol. 20, no. 7, pp. 7119–7127, 2012.

[35] M. Brydegaard *et al.*, "The scheimpflug lidar method. SPIE lidar remote sensing for environmental monitoring," 2017, Art. no. 10406.

[36] E. Malmqvist, M. Brydegaard, M. Aldén, and J. Bood, "Scheimpflug lidar for combustion diagnostics," *Opt. Exp.*, vol. 26, no. 12, pp. 14842–14858, 2018.

[37] Z. Liu *et al.*, "Preliminary studies on atmospheric monitoring by employing a portable unmanned Mie-scattering scheimpflug lidar system," *Remote Sens.*, vol. 11(7), 2019, Art. no. 837.

[38] S. Nakamura, "Background story of the invention of efficient InGaN blue-light-emitting diodes (Nobel lecture)," *Angewandte Chemie Int. Ed.*, vol. 54, no. 27, 2015, pp. 7770–7788.

[39] G. E. Smith, "Nobel lecture: The invention and early history of the CCD," *Rev. Modern Phys.*, vol. 82, no. 3, 2010, Art. no. 2307.

[40] G. Zhao *et al.*, "Inelastic hyperspectral lidar for profiling aquatic ecosystems," *Laser Photon. Rev.*, vol. 10, no. 5, pp. 807–813, 2016.

[41] X. Wang *et al.*, "Drone-based area scanning of vegetation fluorescence height profiles using a miniaturized hyperspectral lidar system," *Appl. Phys. B*, vol. 124, no. 11, 2018, Art. no. 207.

[42] M. Brydegaard, A. Gebru, and S. Svanberg, "Super resolution laser radar with blinking atmospheric particles – application to interacting flying insects," *Prog. Electromagn. Res.*, vol. 147, pp. 141–151, 2014.

[43] L. Mei and M. Brydegaard, "Continuous-wave differential absorption lidar," *Laser Photon. Rev.*, vol. 9, no. 6, pp. 629–636, 2015.

[44] G. Zhao *et al.*, "Inelastic hyperspectral lidar for profiling aquatic ecosystems," *Laser Photon. Rev.*, vol. 10, no. 5, pp. 807–813, 2016.

[45] X. Wang *et al.*, "Drone-based area scanning of vegetation fluorescence height profiles using a miniaturized hyperspectral lidar system," *Appl. Phys. B*, vol. 124, no. 11, pp. 1–5, 2018.

[46] L. Mei and M. Brydegaard, "Atmospheric aerosol monitoring by an elastic scheimpflug lidar system," *Opt. Exp.*, vol. 23, no. 24, pp. A1613–A1628, 2015.

[47] E. Malmqvist, *From Fauna to Flames: Remote Sensing With Scheimpflug Lidar*. Lund, Sweden: Lund University, 2019.

[48] M. Aikio, "Hyperspectral prism-grating-prism imaging spectrograph," 2001.

[49] J. Erdkamp and J. Marriage, "Theodor scheimpflug - The life and work of the man who gave us that rule," *Photograph. World*, vol. 3, no. 3, pp. 29–38, 2012.

[50] G. Høye, T. Løke, and A. Fridman, "Method for quantifying image quality in push-broom hyperspectral cameras," *Opt. Eng.*, vol. 54, no. 5, 2015.

[51] K. Stelmaszczyk *et al.*, "Analytical function for lidar geometrical compression form-factor calculations," *Appl. Opt.*, vol. 44, no. 7, pp. 1323–1331, 2005.

[52] H. Baars *et al.*, "An overview of the first decade of polly NET: An emerging network of automated Raman-polarization lidars for continuous aerosol profiling," *Atmospheric Chem. Phys.*, vol. 16, no. 8, pp. 5111–5137, 2016.

[53] M. Brydegaard *et al.*, "High dynamic range in entomological scheimpflug lidars," *IEEE J. Sel. Topics Quantum Electron.*, vol. 27, no. 4, Jul./Aug. 2021, Art. no. 6900711.

[54] E. Malmqvist *et al.*, "CW-Laser radar for combustion diagnostics," in *Imaging and Applied Optics*. Heidelberg, Germany: Optical Society of America, 2016.

[55] G. Zhao *et al.*, "Particle profiling and classification by a dual-band continuous-wave lidar system," *Appl. Opt.*, vol. 57, no. 35, pp. 10164–10171, 2018.

[56] M. Brydegaard *et al.*, "Short-wave infrared atmospheric scheimpflug lidar," *EDP Sci.*, vol. 176, 2018, Art. no. 4.

[57] T. Tscharntke *et al.*, "Landscape moderation of biodiversity patterns and processes-eight hypotheses," *Biol. Rev.*, vol. 87, no. 3, pp. 661–685, 2012.

[58] J. C. Habel *et al.*, "Butterfly community shifts over two centuries," *Conservation Biol.*, vol. 30, no. 4, pp. 754–762, 2016.

[59] J. C. Biesmeijer *et al.*, "Parallel declines in pollinators and insect-pollinated plants in Britain and The Netherlands," *Sci.,*, vol. 313, no. 5785, pp. 351–354, 2006.
[60] G. D. Powney *et al.*, "Widespread losses of pollinating insects in britain," *Nature Commun.*, vol. 10, no. 1, pp. 1–6, 2019.
[61] E. Mathieu-Bégné *et al.*, "Demographic and genetic collapses in spatially structured populations: Insights from a long-term survey in wild fish metapopulations," *Oikos*, vol. 128, no. 2, pp. 196–207, 2019.
[62] J. Hagler *et al.*, "A method for distinctly marking honey bees, apis mellifera, originating from multiple apiary locations," *J. Insect Sci.*, vol. 11, no. 1, 2011.
[63] R. Hood-Nowotny, L. Mayr, and B. G. Knols, "Use of carbon-13 as a population marker for anopheles arabiensis in a sterile insect technique (SIT) context," *Malaria J.*, vol. 5, no. 1, pp. 1–8, 2006.
[64] E. I. Aviles *et al.*, "Fluorescent markers rhodamine b and uranine for anopheles gambiae adults and matings," *Malaria J.*, vol. 19, no. 1, pp. 1–9, 2020.
[65] T. Mascari and L. Foil, "Laboratory evaluation of the efficacy of fluorescent biomarkers for sugar-feeding sand flies (Diptera: Psychodidae)," *J. Med. Entomol.*, vol. 47, no. 4, pp. 664–669, 2010.
[66] K. Khallaayoune *et al.*, "Attractive toxic sugar baits: Control of mosquitoes with the low-risk active ingredient dinotefuran and potential impacts on nontarget organisms in Morocco," *Environ. Entomol.*, vol. 42, no. 5, pp. 1040–1045, 2013.
[67] D. Howpage, R. Spooner-Hart, and J. Sheehy, "A successful method of mass marking honey bees, apis mellifera, at the hive entrance for field experiments," *J. Apicultural Res.*, vol. 37, no. 2, pp. 91s–997.

Hampus Månefjord was born in Lekeryd, Sweden, in 1992. He received the M.Sc. degree in physics engineering from Lund University, Lund, Sweden, in 2018. The part of his master's education was taken with Nanyang Technological University, Singapore. He is currently working toward the Ph.D. degree in 3D-printed optical instrumentation and biophotonics with the Department of Physics, Lund University.

Lauro Müller was born in Bern, Switzerland, in 1990. He received the B.Sc. degree in micro-and medical technology from the Bern University of Applied Sciences, Bern, Switzerland. He is currently working toward the master's degree in photonics with Lund University, Lund, Sweden. He is also working on his master's Thesis in hyperspectral lidar applications with the Division of Combustion Physics, Lund University.

Meng Li was born Kunming, China, in 1993. She received the M.Sc. degree in photonics in 2018 from Lund University, Lundm, Sweden, where she is currently working toward the Doctoral degree (second-year). Her research focuses on specular reflexes backlasing from insects' flat wings, which report on the membrane thickness for target identification.

Jacobo Salvador was born in Buenos Aires, Argentina, in 1976. He received the Electronic Engineering degree and the Ph.D. degree in image and signal processing from National Technological University, Buenos Aires, Argentina, in 2007 and 2011, respectively. He specialized in embedded system with Buenos Aires University, Buenos Aires, Argentina, in 2020.

Sofia Blomqvist was born in Ronneby, Southern Sweden, in 1992. She received the M.Sc. degree in conservation biology with Lund University, Lund, Sweden. She is currently working toward the Ph.D. degree in environmental science with the Centre for Environmental and Climate Science, Lund, with focus on pollinating insects in road verges.

Anna Runemark was born in Karlskrona, Sweden, in 1982. She received the M.Sc. degree in biology from Uppsala University, Uppsala, Sweden, in 2007, and the Ph.D. degree in evolutionary ecology from Lund University, Lund, Sweden, in 2012. She completed the Postdoctoral studies from the Centre for Ecological and Evolutionary Synthesis, University of Oslo, Oslo, Norway. She is currently an Associate Senior with the Department of Biology, Lund University.

Carsten Kirkeby was born Køge, Denmark, in 1980. He received the M.Sc. degree in biology from the University of Copenhagen, Copenhagen, Denmark, in 2007, and the Ph.D. degree in epidemiology of *Culicoides* from the Technical University of Denmark, Denmark, in 2013.

Rickard Ignell was born in Dalby, Sweden, in 1969. He received the M.Sc. degree in animal ecology and the Ph.D. degree in chemical ecology from Lund University, Lund, Sweden. He is currently the PI of the Disease Vector Group, Swedish University of Agricultural Sciences, Uppsala, Sweden, which focuses on the ecology, particularly the chemical ecology, of disease transmitting mosquitoes.

Joakim Bood was born in Norrköping, Sweden, in 1967. He received the M.Sc. and Ph.D. degree in physics from Lund University, Lund, Sweden, in 1995 and 2000, respectively. From 2001 to 2003, he was a Postdoc with Sandia National Laboratories, Albuquerque, NM, USA. Since 2017, he has been a Full Professor with Lund University, where he is running a research program focused on short-pulse (ps/fs) spectroscopy, applied molecular spectroscopy, and remote sensing.

Mikkel Brydegaard was born in Copenhagen, Denmark, in 1980. He received the M.Sc. degree in electrical engineering, and the Ph.D. degree in atomic physics, biophotonics, and remote sensing from Lund University, Lund, Sweden, in 2007 and 2012, respectively. He is/was a Postdoctoral Research with Stellenbosch University, Stellenbosch, South Africa and Norsk Elektro Optikk, Oslo, Norway. He was the recipient of the Inaba prize 2014, Docent 2016, and ERC awardee 2018. Since 2021, he has been a Senior lecturer with Lund University. He is/was the Co-founder of the African Spectral Imaging Network and Fauna Photonics, Denmark.